

Boosting tunable blue luminescence of halide perovskite nanoplatelets through post-synthetic surface trap repair

Bernhard J. Bohn,^{1,2,#} Yu Tong,^{1,2,#} Moritz Gramlich,^{1,2} May Ling Lai,³ Markus Döblinger,⁴ Kun Wang,⁵ Robert L. Z. Hoye,³ Peter Müller-Buschbaum,⁵ Samuel D. Stranks,³ Alexander S. Urban,^{1,2,*} Lakshminarayana Polavarapu,^{1,2,*} and Jochen Feldmann^{1,2,*}

¹ Chair for Photonics and Optoelectronics, Department of Physics and Center for NanoScience (CeNS), Ludwig-Maximilians-Universität München, Amalienstr. 54, 80799 Munich, Germany

² Nanosystems Initiative Munich (NIM), Schellingstr. 4, 80799 Munich, Germany

³ Cavendish Laboratory, JJ Thomson Avenue, Cambridge CB3 0HE, United Kingdom

⁴ Department of Chemistry, Ludwig-Maximilians-Universität München, Butenandtstr. 5-13 (E), 81377 Munich, Germany

⁵ Lehrstuhl für Funktionelle Materialien, Physik Department, Technische Universität München. James-Frank-Str. 1, 85748 Garching, Germany

equal contribution

* corresponding authors: urban@lmu.de, l.polavarapu@lmu.de, feldmann@lmu.de

KEYWORDS: CsPbBr₃, perovskite nanocrystals; nanoplatelets; quantum confinement; exciton binding energy; defect passivation; blue light emitting diodes

ABSTRACT:

The easily tunable emission of halide perovskite nanocrystals throughout the visible spectrum makes them an extremely promising material for light-emitting applications. Whereas high quantum yields and long-term colloidal stability have already been achieved for nanocrystals emitting in the red and green spectral range, the blue region currently lags behind, with low quantum yields, broad emission profiles and insufficient colloidal stability. In this work, we present a facile synthetic approach for obtaining two-dimensional CsPbBr₃ nanoplatelets with monolayer-precise control over their thickness, resulting in sharp photoluminescence and electroluminescence peaks with a tunable emission wavelength between 432 and 497 nm due to quantum confinement. Subsequent addition of a PbBr₂-ligand solution repairs surface defects likely stemming from bromide and lead vacancies in a sub-ensemble of weakly emissive nanoplatelets. The overall photoluminescence quantum yield of the blue-emissive colloidal dispersions is consequently enhanced up to a value of 73±2 %. Transient optical spectroscopy measurements focusing on the excitonic resonances further confirm the proposed repair process. Additionally, the high stability of these nanoplatelets in films and to prolonged UV light exposure is shown.

Halide perovskites in the form of bulk thin films have attracted significant interest owing to rapid rises in photovoltaic efficiencies.¹⁻⁵ Nanocrystals (NCs) of the same material have been garnering strong interest since 2014 for light emission applications due to high photoluminescence quantum yields (PLQYs) approaching unity and an emission wavelength that is tunable throughout the visible range by changing the halide ion.⁶⁻¹⁴ Two of the important limitations currently hindering the widespread use of this material, are i) a very low efficiency of chloride-containing perovskite NCs, and thus only poor performance in the blue spectral range and ii) a tendency of mixed-halide perovskite to phase segregate into domains with different halide ion contents and resulting bandgaps, consequently shifting the emission wavelength strongly during operation of LEDs.¹⁵⁻²⁰ While most of these NCs are either bulk-like or only weakly confined, several studies have shown strong quantum confinement in perovskite NCs as a further viable method to tune the emission

wavelength especially towards the blue-spectral range.²¹⁻²³ In particular, two-dimensional (2D) nanoplatelets (NPIs) have been demonstrated with an atomic-precision control over their thickness down to a single monolayer (ML) and large exciton binding energies, an appealing characteristic for light-emitting applications.^{15, 24-30} These NPIs are unfortunately strongly susceptible to surface defects due to a large surface-to-volume ratio, rendering their QYs typically quite low.^{18, 23, 25, 26, 31} It was often observed that the PLQY of both hybrid and inorganic perovskite NCs drastically decreases with the change in morphology from cubic to platelet form.^{23, 24, 26, 32} For instance, the PLQY of CsPbBr₃ NCs drops from 78 % to 31 % with a change of morphology from cubic to thick NPIs.^{23, 24} Additionally, it is difficult to produce NPIs of only a single thickness using current synthesis routes, and the resulting NPIs tend to have problems with long-term stability.^{18, 26, 33-35}

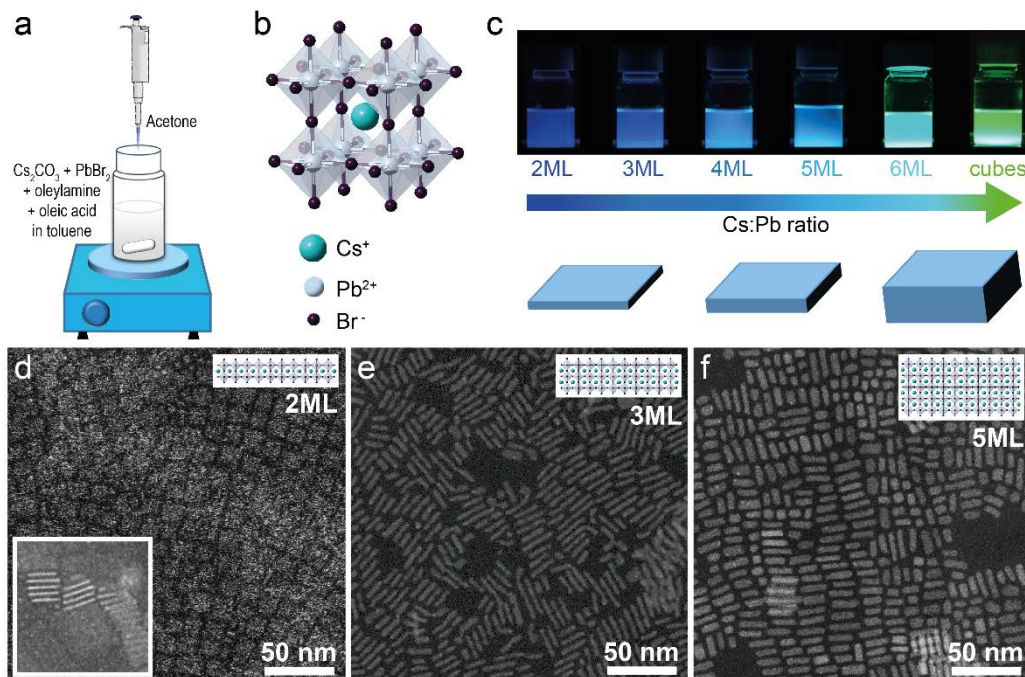


Figure 1. (a) Schematic illustration showing the synthesis of CsPbBr₃ nanoplatelets by reprecipitation of precursors using acetone. **(b)** Cubic crystal structure of CsPbBr₃ perovskite NCs. **(c)** Photographs of vials containing the colloidal NPI dispersions (obtained with increasing Cs:Pb ratio) illuminated with UV-light. A steady redshift with increasing ML thickness can be observed. **(d)-(f)** HAADF-STEM images of 2ML, 3ML and 5ML NPIs.

In this work, we present a simple room temperature synthesis method for obtaining blue-emitting colloidal CsPbBr₃ NPIs with precisely controllable thickness from 2 to 6 MLs. All NPIs exhibit clear excitonic peaks in absorption spectra – a result of the increased exciton binding energies in these confined nanostructures – as well as narrow photoluminescence (PL) and electroluminescence (EL) emission. We show that the PLQYs of these NPIs can be significantly enhanced through a post-synthetic treatment by the addition of a PbBr₂-ligand solution. The PLQYs of these NPIs reach up to 73±2 % with the emission color retained, making this NPI series one of the most efficient perovskite blue light-emitters reported to date.³⁶ Transient absorption spectroscopy (TAS) and time-resolved (TR)-PL studies reveal that the enhancement affects a sub-ensemble of the NPIs for which surface defects – initially hindering radiative recombination – are repaired, enhancing the overall emission of the NPI dispersions. Additionally, we show the enhanced stability of the NPIs even under prolonged UV exposure. The synthesis of CsPbBr₃ NPIs applies the concept of reprecipitation³⁷ with thickness control achieved by regulating the molar ratio of the precursors, as in our previous studies (see Figure 1a-

c).^{11, 24} Briefly, a Cs-oleate precursor with a specific Cs:Pb ratio for each NPI thickness (cf. Supporting Information Table S1) was added into a toluene solution containing a PbBr₂-oleylamine/oleic acid precursor at room temperature under vigorous stirring (Figure 1a). After 5s, a large amount of acetone was added to initiate formation of the NPIs. The reaction was then run for 1 min under continuous stirring, after which the mixture was centrifuged for 3 min and then redispersed in 2 ml of hexane. The thickness of the NPIs was controlled by varying the ratio of the Cs:Pb precursors and the amount of acetone added. The details of the synthesis are given in the Supporting Information (Materials and Methods). The resulting dispersions show a strong difference in color, especially under UV-light, with a clear shift from blue to green with increasing Cs:Pb ratio (see Figure 1c). This is indicative of quantum confinement effects and very similar to our previous findings on hybrid organic-inorganic perovskites, where the MA:Pb ratio was controlled.²⁴ In these two approaches the amount of the A-site cation (here: Cs⁺, previously MA⁺) is decreased with respect to the other precursors, limiting the amount of perovskite that can be formed and the resulting nanocrystals shrink in size or more specifically in thickness. Thus, NPIs with thicknesses down to a single monolayer can be formed. However, one drawback of our previous approach was that the syntheses tended to form NPIs dispersions of mixed thicknesses leading to broad PL emission. To investigate the monodispersity of the NCs in our new findings, we employed annular dark field scanning transmission electron microscopy (ADF-STEM) as shown in Figure 1d-f. For the lowest Cs:Pb ratio, we find regularly sized, low contrast square-shaped NCs with side lengths of 14±4 nm (Figure 1d). The low-contrast signifies very thin NPIs, which is confirmed by images of NPIs standing on their side (see inset), from which we measured a thickness of 1.2±0.1 nm. One ML in this case signifies a 2D arrangement of corner-sharing [PbBr₆]⁴⁻ octahedra with a thickness of 0.59 nm (Figure 1b).^{11, 12} Therefore, the measured thickness likely corresponds to NPIs comprising two MLs. As the Cs:Pb ratio increases, the thickness of the NPIs also increases (2.0±0.3 nm and 2.9±0.3 for the 3ML and 5ML NPIs, respectively. See Figure 1d-f and also Figure S1 for a detailed analysis of the thickness). Additionally, we find that the lateral size is nearly constant for all of the NPI samples (cf. Figures S1, S2). ADF-STEM imaging and corresponding fast Fourier transform (FFT) patterns confirm the high level of crystallinity of the NPIs, which exhibit an orthorhombic or cubic crystal structure (cf. Figure S5). Additionally, inferred from the higher optical contrast, we observe a strong tendency of the NPIs to arrange in stacks along the substrates, signifying a high uniformity in the lateral size of the nanoplatelets.³⁸ This stacking does not happen in the dispersions, as derived from the lack of any precipitate forming and nearly no scattering observed in the UV-VIS spectra. From these analyses, it seems as if the dispersions contain NPIs each with only one specific thickness ranging from 2 - 6 MLs. This is further confirmed by X-ray diffraction (XRD) analysis. Additionally to the bulk CsPbBr₃ 00l peaks, which signify a high degree of orientation of the NPIs, peaks resulting from stacking of the NPIs are observed (cf. Figure S7). Using these, we obtain spacing values between individual NPIs, which correspond well to the expected thickness of the inorganic layer including a ligand length of 1.5nm surrounding the NPIs.

In order to confirm this, we turned to optical spectroscopy, probing the linear PL and absorption spectra of each NPI dispersion (Figure 2a,b). Each PL spectrum clearly comprises only a single narrow peak (full width at half-maximum (FWHM) down to 11 nm), with the central peak position blueshifting from 515 nm to 432 nm with decreasing Cs:Pb ratio in the precursor (Figure 2a). The Cs:Pb ratio used to obtain the 515 nm emission wavelength is comparable to those we used previously to obtain weakly quantum-confined nanocubes.^{11, 39} The absorption spectra of all NPI samples show a clear absorption onset, with small Stokes shifts of 6 - 10 nm (Figure 2a). Additionally, as the Cs:Pb ratio is reduced, a clear excitonic absorption peak can be observed and for the lowest ratios, additionally a step-like increase resembling the continuum onset of a 2D semiconductor (Figure 2b). With the spectra being acquired at room temperature, the emergence of the excitonic resonance signifies that the exciton binding energy E_B increases with decreasing Cs:Pb ratio, to

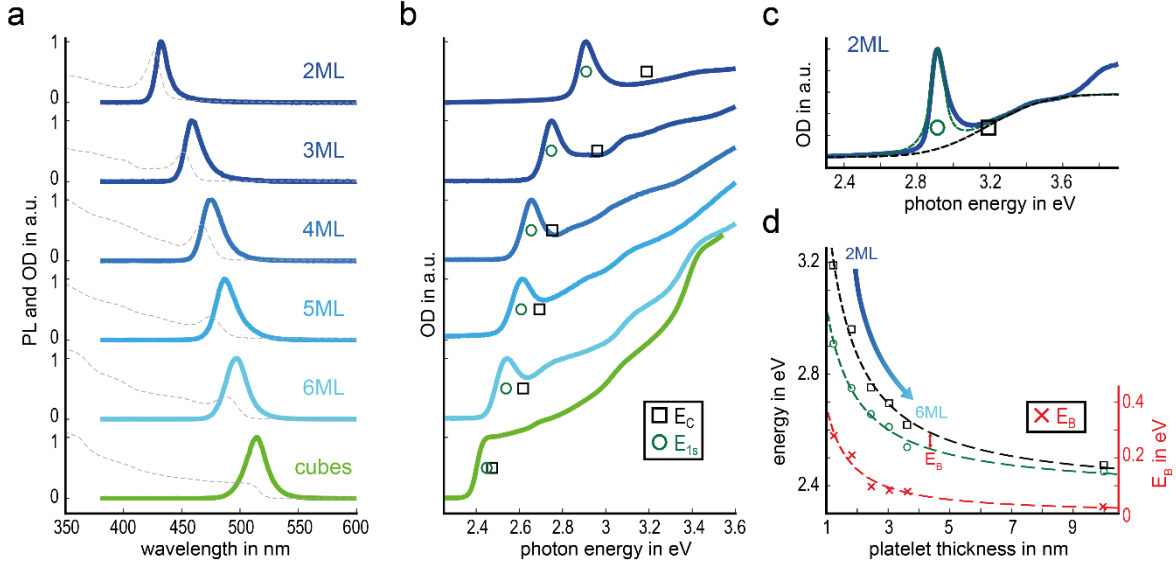


Figure 2. (a) Photoluminescence (solid lines) and absorption (dashed lines) spectra of NPI colloids for varying NPI thickness. Spectra of weakly-confined nanocubes are also shown for comparison. (b) Absorption spectra normalized to the excitonic peak. Green circles indicate the energetic position of the exciton transition E_{1s} and black squares show the corresponding continuum absorption onset E_C for each sample. (c) Model (green dashed line) applied to extract these positions from the experimental data (solid curve, in this case 2ML) using the excitonic peak and the absorption onset of the continuum (black dashed line). (d) The obtained values for E_C and E_{1s} versus the NPI thickness. Their difference is the exciton binding energy E_B (red crosses), which increases strongly with decreasing NPI thickness. Dashed lines are added as guides to the eye.

an extent that the thermal energy at room temperature is progressively less able to dissociate excitons. As it can be seen in Figure 2b additional peaks emerge at higher photon energies, however, these stem from transitions between higher energetic bands and are not considered further.⁴⁰ Similar widths of excitonic absorption peaks and PL emission spectra, small Stokes shifts and the lack of additional peaks in the PL spectra all support the hypothesis that the dispersions actually comprise NPIs of only a single thickness. Accordingly, we confirm the correlation of the observed PL peaks and corresponding dispersions to NPIs with a ML thickness of $n = 2$ up to $n = 6$.¹²

The observed blueshift in the PL spectrum with decreasing Cs:Pb ratio stems from quantum-confinement in the NPIs. This effect generally results in the increase of the continuum absorption onset E_C given by the respective band gap energy of the bulk crystal and the confinement energies of the electron and hole, $E_C = E_G + E_e + E_h$. The exciton binding energy E_B increases simultaneously. As these effects actually shift the resulting PL emission in opposite directions, the shift of E_C must be larger than the increase of E_B in order to induce the observed blueshift. To confirm this, we have modelled the absorption spectra using Elliot's model (Figure 2c). Using a method similar to that suggested by Naem et al. for 2D platelets,⁴¹ we can assign the continuum absorption onset energy E_C (black squares) and also the energetic position of the dominant $1s$ excitonic transition E_{1s} (green circles) to each of the samples in Figure 2b by modeling the contribution of the excitonic peak and the lowest band of the continuum transitions. These values are important, as their difference is exactly the exciton binding energy: $E_B = E_C - E_{1s}$. This model can be applied through a simple modification to 2D and 3D semiconductors, which apply for the 2 ML and the cube case, respectively. For all other NPIs, the actual structure is somewhere in between, as they are only "quasi-2D" due to their finite thicknesses. Yet, they are also not three-dimensional due to a significant degree of quantum confinement in

one direction. We were able to extract values for all NPI thicknesses, which we have plotted in Figure 2d. Clearly, both energies decrease with increasing NPI thickness. The exciton binding energy E_B , being the difference between the two curves can be seen to increase as the NPI thickness is reduced, reaching a value of 280 meV for the 2ML case. This is nearly 10 times the value for the cubes of only 30 meV, which corresponds well to previously described values.⁴²⁻⁴⁵ This strong change can be understood when comparing the excitonic Bohr radius of bulk CsPbBr_3 , reported to be approximately $a_B = 7$ nm, with the NPI thickness. Clearly, the 2 to 6 ML NPIs are far thinner than this, thus they are in the limit of strong quantum-confinement, while the cubes with a side length of about 10 - 12 nm are only in the weak limit.²² Previously it has been shown that the extraction of E_B by analysis of absorption data is prone to fitting ambiguities in the case of bulk perovskite crystals⁴⁶ and other approaches have been applied to extract this value.^{42, 47} However, here in the case of strong confinement for the NPI dispersions with clearly separated excitonic and continuum absorption, the fitting of absorption data is significantly more reliable.

While the synthesis yields perovskite NPIs with uniform thickness and narrow PL emission spectra, the intensity, especially for the thinnest NPIs tends to be quite low. In fact, for the 2ML and 3ML samples we determine their PLQY to be only around 7 ± 1 % and 9 ± 1 %, respectively. Such low values have commonly been observed and are likely a result of the existence of surface trap states and the high surface-to-volume ratio of these 2D nanostructures.^{23, 25} To address this issue, we have developed a post-synthetic treatment of the colloidal NPIs obtained from the previously described synthesis in order to passivate the trap states on the NPI surface. We discovered that by adding a PbBr_2 -ligand (oleic acid and oleylamine) hexane solution to the NPI dispersion, we can dramatically enhance their PLQYs. Immediately after addition, the PL of the samples is strongly increased, so that the dispersions appear deeply blue even under ambient lighting (see Figure S9). It turns out that the PL intensity of each NPI dispersion can be significantly enhanced, as shown in Figure 3a. The PL peak maxima and absorption features were nearly constant, with some samples showing only minor blueshifts (10-15 meV) after the enhancement. This could be due to an increasing of the dielectric constant of the enhanced samples and a blueshift of the excitonic resonance position due to the increased Coulomb screening. These results indicate that the treatment enhances the PL efficiency of the colloidal NPIs without affecting their thickness or uniformity, as confirmed through ADF-STEM imaging and XRD measurements (cf. Figures S3 and S8). Furthermore, electron diffraction measurements show that the crystallinity of the NPIs is significantly increased in the enhanced samples (see Figures S4 and S5). Energy-dispersive X-ray (EDX) spectroscopy shows additionally that the ratio of Br:Pb and Pb:Cs ions in the NPIs increases as a result of the enhancement (see Supporting Information for details, Figure S6). To investigate the mechanism, for comparison, we added a similar solution without the PbBr_2 (only the organic ligands in hexane) to the NPI dispersions. As in our previous work, we find that the dilution and additional ligands tend to decompose the NPIs, in this case mainly into their original precursors, as determined through PL spectroscopy (see Figure S10). Furthermore, we applied various additional bromide-salt-ligand solutions (SnBr_2 , KBr, NaBr) in the enhancement step. All of these lead to an enhancement of the PL, albeit of smaller magnitude than for the PbBr_2 -solution (see Figure S11). These results together imply that Br and Pb vacancies at the surface of the nanocrystals are filled by the enhancement solution, with the ligands serving to passivate any uncoordinated surface atoms (see Figure 3b).

The enhancement is effective for all thicknesses from 2 to 6 ML with PLQY values of 7 ± 1 % and 42 ± 3 % for the 2 and 6 ML samples before and 49 ± 3 % and 73 ± 2 % after the enhancement process (Figure 3c). The PLQY values of 49 ± 3 % (2ML) and 60 ± 4 % (3ML) are one of the highest reported PLQYs of any perovskite material for an emission wavelength shorter than 470 nm. Interestingly, we observe that the degree of enhancement

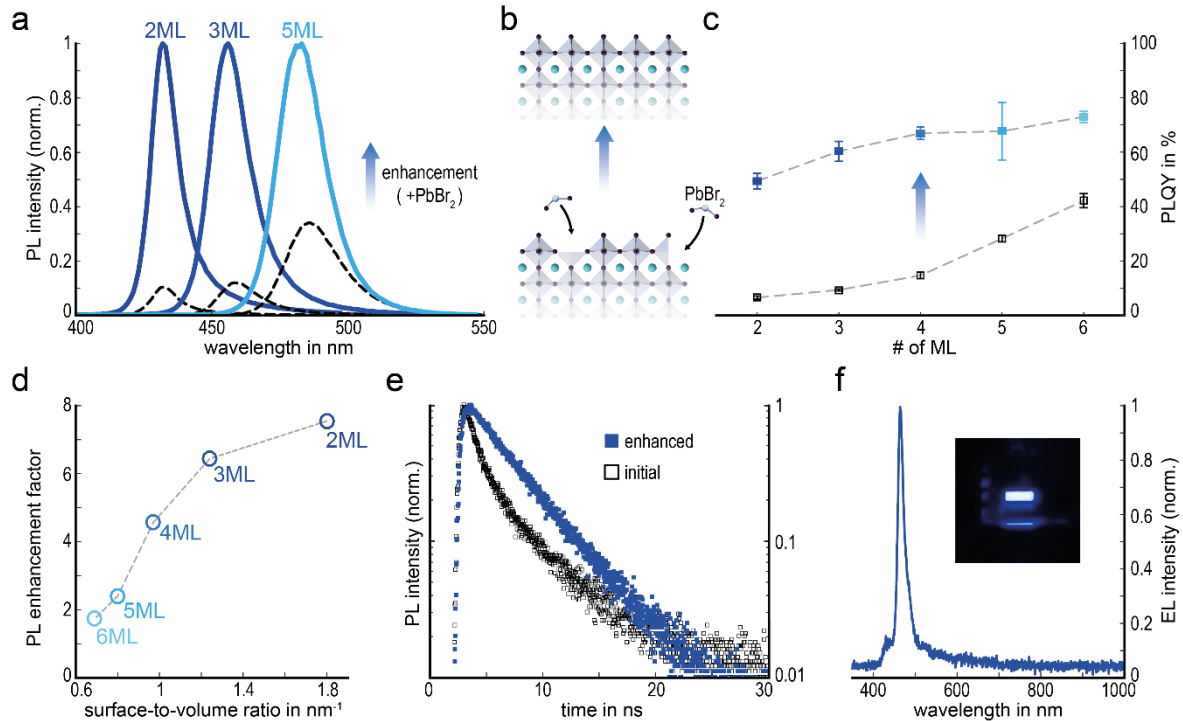


Figure 3. (a) PL spectra of initial NPI colloidal dispersions (black dashed lines) and enhanced dispersions (normalized, solid lines). (b) Scheme for the repair process of surface defects initiated by a chemical post-treatment with a PbBr_2 solution. (c) PLQYs of the NPL dispersions pre-enhancement (open black squares) and post-enhancement (full blue squares). $n \geq 6$ values have been averaged for each data point. Dotted lines are guides to the eye. (d) PL enhancement factor as a function of the surface-to-volume ratio. (e) TR-PL of a 3ML NPI dispersion before (open black squares) and after enhancement (full blue squares). (f) Electroluminescence (EL) spectrum of a light-emitting diode (LED) based on the enhanced 3ML NPIs. Inset: photo of the working LED.

is strongly dependent on the thickness of the sample, with the PLQYs improving by a much larger factor for the thinnest platelets (Figure 3d). In fact, there seems to be a strong monotonically-increasing dependence of the enhancement factor on the surface-to-volume ratio. The enhanced NPIs also turn out to be extremely stable, as colloidal dispersion retain 90 % of their PL intensity after 10 days (cf. Figure S12) and films obtained through spin-coating retained more than 85 % of their PL intensity even after continuous illumination with UV-light for six hours (see Figure S13). Additionally, when investigating the PL lifetimes of the NPI samples, we find that not only does the lifetime increase after the enhancement procedure (e.g. $\tau_{1/e}$ from 1.7 to 4.1 ns for the 3ML sample), but the shape of the decay also strongly changes (see Figure 3e, cf. Supporting Information including Figures S14 and S15). While the decay curve of the initial, non-enhanced samples can only be reproduced through a multiexponential function, the decay of all the enhanced NPI samples becomes monoexponential. Finally, we demonstrate that the passivation route can yield blue EL when incorporated in a light emitting-diode (LED) device structure (Figure 3f). The LED device based on the 3ML NPIs shows pure blue emission with a single, narrow EL peak (FWHM < 20 nm) centered at 464 nm, close to that of the PL (see Supporting Information for more details on the device fabrication and performance, Figure S16). The combination of a narrow emission linewidth and a pure blue color demonstrate their strong potential for use in high-performance LED applications.^{19, 48, 49}

To get a deeper understanding of this enhancement procedure one has to consider that semiconductor nanocrystals are known to be highly prone to surface traps, as the atoms/ions sitting at the edges are undercoordinated, leaving dangling bonds.⁵⁰ For larger perovskite nanocrystals in the unconfined or weakly

quantum confined regimes, surface passivation is highly effective, often leading to extremely high PLQY values approaching unity. On the other hand, strongly confined NCs, for example 2D NPIs, tend to have significantly lower QYs. One reason for this could be due to them possessing a higher surface-to-volume ratio, which could render them more susceptible to surface defects. Additionally, the reduced thickness also leads to a reduced dielectric screening, as witnessed by the strongly increased exciton binding energies. This will likely also increase scattering rates of excitons with defects and polar optical phonons, enhancing nonradiative recombination.²⁸ Such is the case for the NPIs obtained through the synthesis before the enhancement step. As a side note, the enhancement process also works for the nanocubes, even though the enhancement factor is far less due to the extremely high QYs of the initial nanocubes (approx. 92 %). This supports the notion of surface traps being the reason for the reduced QYs for thinner NPIs. Interestingly, the shape of the PL decay suggests that the NPIs are split into two sub-ensembles (see Figure 4a). One ensemble without surface defects and a high QY and one ensemble with surface defects and strongly reduced or no emission. The enhancement renders a larger fraction of the NPIs emissive, and thus the PL decay becomes dominated by excitonic recombination and not by non-radiative, trap-mediated decay. This also explains why the enhancement is more effective for the thinner NPIs, as surface defects affect them more, increasing a chance that a NPI will be non-emissive.

In order to validate this model and the dramatic increase in the PLQY, we employ transient absorption spectroscopy (TAS). The NPIs in solution are spaced relatively far apart and so do not exchange excited charge carriers. Thus, in solution, each NPI can be considered independent of the other NPIs. If a NPI in the ensemble is photoexcited, it can contain one or multiple electron hole pairs, which rapidly relax down to the 1s exciton state. For the case of multiple excitations, fast non-radiative exciton-exciton annihilation dominates the recombination of the charge carriers,^{51, 52} until only one exciton per photoexcited platelet remains. Now, in a defect-free NPI the excited electron hole pair tends to recombine radiatively (light colored platelet in Figure 4a), whereas the excitation in a NPI with defects has the possibility to recombine radiatively by sending out a photon or non-radiatively via the defect-induced trap states (dark platelet in Figure 4a).

Figure 4b,c show the steady state absorption of the 3ML sample and the respective TAS spectra for an excitation at 400 nm (≈ 3.1 eV) with a dominant bleaching peak at around 452 nm, corresponding to the excitonic peak in the steady state absorption, well below the continuum onset E_c . To study the effect of the post-synthetic enhancement on the dynamics of the differential absorption at the energetic position of the exciton, we look at three different colloidal dispersions of 3ML NPIs: one before enhancement (initial), one with full enhancement (enhanced), and one where only half the necessary amount of PbBr₂ was added and a reduced enhancement is observed (partially enhanced). Figure 4d,e show the transients of differential transmission at the energetic position of the exciton for the initial and the enhanced case.

As proposed above and shown in Figure 4a, we consider there to be two sub-ensembles of platelets in each NPI dispersion. As a consequence the transients in Figure 4d,e represent a superposition of the transient absorption signal of the two sub-ensembles for both cases, the initial and the enhanced sample. As indicated by the black lines, these two transients behave very similar on the very short ($t_{\text{delay}} < 50$ ps) and very long time scales ($t_{\text{delay}} > 500$ ps), however, a significantly different behavior can be observed in the intermediate time regime. With the long timescale process likely being due to recombination, as it is describable through a single exponential function (excitonic recombination), we subtract it from the curves in order to compare the two shorter timescale processes.

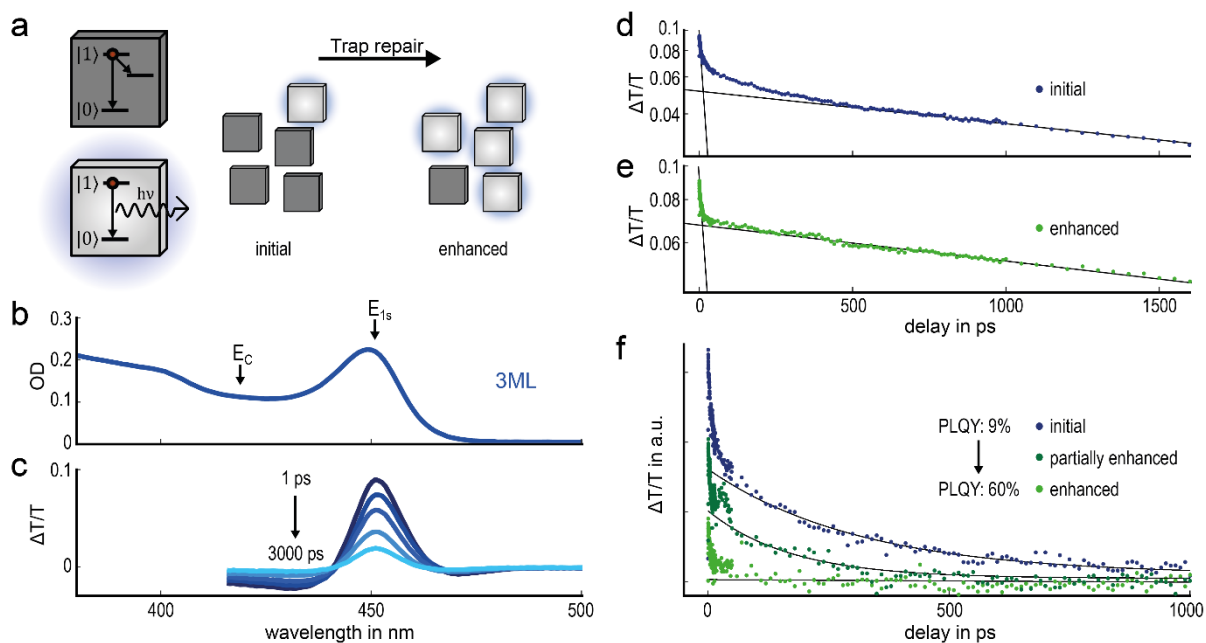


Figure 4. (a) Scheme depicting the post-synthetic trap repair and concomitant increase of the number of defect-free nanoplatelets that exhibit predominantly radiative recombination. (b) Steady-state absorption spectrum and (c) differential absorption spectra at delay times ranging from 1 to 3000 ps after excitation for the 3ML sample. (d) Transients of differential absorption at the energetic position of the exciton, as shown in (b) for an ensemble of (d) an initial and of (e) an enhanced 3ML sample. (f) Transients after subtracting the late time decay corresponding to excitonic recombination. The initial samples show exciton trapping in non-emissive NPIs with surface defects as an additional process, which is slower than exciton-exciton annihilation, but faster than excitonic recombination.

After subtracting the late time component, the bleaching decay curves show two main processes happening in the first nanosecond after excitation (see Figure 4f). An initial very fast decay is observed, which we attribute to non-radiative exciton-exciton annihilation, as it exhibits a strong dependency on the excitation density. During the time of the second decay component ($50 \text{ ps} < t_{\text{delay}} < 500 \text{ ps}$) a large part of the excitation is lost in the initial sample (dark blue). This amount is substantially reduced in the partially enhanced sample and not observable in the fully enhanced sample. Therefore, we conclude that this decay component stems from a decay channel not present in the enhanced NPIs – namely the non-radiative recombination via surface trap states in the sub-ensemble containing defects. This is strong support for the concept of the reduction of surface traps by post-synthetic enhancement with PbBr_2 leading to a larger sub-ensemble of defect-free NPIs exhibiting strong radiative recombination.

In conclusion, we have shown a facile synthetic approach to obtain colloidal CsPbBr_3 NPIs with an atomic layer level control of the thickness and with high PLQYs. The NPIs, which range in thickness from 2 - 6 MLs all exhibit narrow PL emission in the blue color range as well as sharp excitonic absorption peaks. Through linear optical spectroscopy we confirm that all NPIs lie in the strong quantum confinement regime with exciton binding energies up to 280 meV. The high PLQYs of the NPIs are achieved through a post-synthetic treatment of the NPI dispersions with a PbBr_2 -ligand addition. TR-PL and TAS substantiate our proposition that this strong increase in PL is induced by surface trap repair of bromide and lead vacancies in the NPIs. This is also the reason why the enhancement process affects the thinnest platelets with a large surface-to-volume ratio in the strongest fashion. This renders the post-processed colloidal NPIs exhibiting a high PLQY in the range of 50 % - 75 %, amongst the most efficient, tunable blue-emitting perovskites to date. As shown in a proof-of-

concept experiment these NPIs could be ideal candidates for blue emitting LEDs, opening the door for all-perovskite white LEDs and other light-emitting applications.

SUPPORTING INFORMATION:

Materials and Methods for Synthesis and the Enhancement procedure; Morphological and structural characterization: Transmission electron microscopy (TEM), Electron diffraction, High-resolution annual darkfield scanning tunneling electron microscopy (HR-ADF-STEM), Energy-dispersive X-ray (EDX) spectroscopy, X-ray Diffraction (XRD); Optical Characterization: UV-Vis, PL spectroscopy, time resolved (TR) PL spectroscopy; LED fabrication and electroluminescence (EL) measurements.

ACKNOWLEDGEMENTS:

This research work was supported by the Bavarian State Ministry of Science, Research, and Arts through the grant “Solar Technologies go Hybrid (SolTech),” by the European Research Council Horizon 2020 ERC Grant Agreement No. 759744 - PINNACLE (A.S.U.), by the China Scholarship Council (Y.T. and K.W.), by the European Union’s Horizon 2020 research and innovation program under the Marie Skłodowska-Curie Grant Agreement COMPASS No. 691185 and by LMU Munich’s Institutional Strategy LMU excellent within the framework of the German Excellence Initiative (A.S.U. and L.P.). R.L.Z.H. would like to acknowledge support from Magdalene College, Cambridge. S.D.S acknowledges funding from the European Research Council (ERC) under the European Union’s Horizon 2020 research and innovation programme (grant agreement number 756962), and the Royal Society and Tata Group (UF150033). B.J.B. and Y.T. contributed equally to this work. The authors would like to thank Sebastian Rieger for helpful discussions.

REFERENCES:

1. Chung, I.; Lee, B.; He, J. Q.; Chang, R. P. H.; Kanatzidis, M. G. *Nature* **2012**, 485, 486-489.
2. Stranks, S. D.; Snaith, H. J., Perovskite Solar Cells. In *Photovoltaic Solar Energy*, 2017; pp 277-291.
3. Kamat, P. V. *ACS Energy Lett.* **2017**, 3, 28-29.
4. Yang, W. S.; Park, B.-W.; Jung, E. H.; Jeon, N. J.; Kim, Y. C.; Lee, D. U.; Shin, S. S.; Seo, J.; Kim, E. K.; Noh, J. H.; Seok, S. I. *Science* **2017**, 356, 1376-1379.
5. NREL Research Cell Record Efficiency Chart. (accessed Apr 18, 2018),
6. Schmidt, L. C.; Pertegas, A.; Gonzalez-Carrero, S.; Malinkiewicz, O.; Agouram, S.; Espallargas, G. M.; Bolink, H. J.; Galian, R. E.; Perez-Prieto, J. *J. Am. Chem. Soc.* **2014**, 136, 850-853.
7. Nedelcu, G.; Protesescu, L.; Yakunin, S.; Bodnarchuk, M. I.; Grotevent, M. J.; Kovalenko, M. V. *Nano Lett.* **2015**, 15, 5635-5640.
8. Protesescu, L.; Yakunin, S.; Bodnarchuk, M. I.; Krieg, F.; Caputo, R.; Hendon, C. H.; Yang, R. X.; Walsh, A.; Kovalenko, M. V. *Nano Lett.* **2015**, 15, 3692-3696.
9. Akkerman, Q. A.; D’Innocenzo, V.; Accornero, S.; Scarpellini, A.; Petrozza, A.; Prato, M.; Manna, L. *J. Am. Chem. Soc.* **2015**, 137, 10276-10281.
10. Gonzalez-Carrero, S.; Francés-Soriano, L.; González-Béjar, M.; Agouram, S.; Galian, R. E.; Pérez-Prieto, J. *Small* **2016**, 12, 5245-5250.
11. Tong, Y.; Bladt, E.; Aygüler, M. F.; Manzi, A.; Milowska, K. Z.; Hintermayr, V. A.; Docampo, P.; Bals, S.; Urban, A. S.; Polavarapu, L.; Feldmann, J. *Angew. Chem. Int. Ed.* **2016**, 55, 13887-13892.

12. Polavarapu, L.; Nickel, B.; Feldmann, J.; Urban, A. S. *Adv. Energy Mater.* **2017**, *7*.
13. Koscher, B. A.; Swabeck, J. K.; Bronstein, N. D.; Alivisatos, A. P. *J. Am. Chem. Soc.* **2017**, *139*, 6566-6569.
14. Song, J. Z.; Li, J. H.; Li, X. M.; Xu, L. M.; Dong, Y. H.; Zeng, H. B. *Adv. Mater.* **2015**, *27*, 7162-7167.
15. Bekenstein, Y.; Koscher, B. A.; Eaton, S. W.; Yang, P. D.; Alivisatos, A. P. *J. Am. Chem. Soc.* **2015**, *137*, 16008-16011.
16. Kumar, S.; Jagielski, J.; Yakunin, S.; Rice, P.; Chiu, Y.-C.; Wang, M.; Nedelcu, G.; Kim, Y.; Lin, S.; Santos, E. J. G.; Kovalenko, M. V.; Shih, C.-J. *ACS Nano* **2016**, *10*, 9720-9729.
17. Li, G.; Price, M.; Deschler, F. *APL Mater.* **2016**, *4*, 091507.
18. Ravi, V. K.; Swarnkar, A.; Chakraborty, R.; Nag, A. *Nanotechnology* **2016**, *27*.
19. Congreve, D. N.; Weidman, M. C.; Seitz, M.; Paritmongkol, W.; Dahod, N. S.; Tisdale, W. A. *ACS Photonics* **2017**, *4*, 476-481.
20. Lignos, I.; Protesescu, L.; Emiroglu, D. B.; Maceiczkyk, R.; Schneider, S.; Kovalenko, M. V.; deMello, A. J. *Nano Lett.* **2018**, *18*, 1246-1252.
21. Huang, H.; Liu, M.; Li, J.; Luo, L.; Zhao, J.; Luo, Z.; Wang, X.; Ye, Z.; He, H.; Zeng, J. *Nanoscale* **2017**, *9*, 104-108.
22. Butkus, J.; Vashishtha, P.; Chen, K.; Gallaher, J. K.; Prasad, S. K. K.; Metin, D. Z.; Laufersky, G.; Gaston, N.; Halpert, J. E.; Hodgkiss, J. M. *Chem. Mater.* **2017**, *29*, 3644-3652.
23. Akkerman, Q. A.; Motti, S. G.; Srimath Kandada, A. R.; Mosconi, E.; D'Innocenzo, V.; Bertoni, G.; Marras, S.; Kamino, B. A.; Miranda, L.; De Angelis, F.; Petrozza, A.; Prato, M.; Manna, L. *J. Am. Chem. Soc.* **2016**, *138*, 1010-1016.
24. Sichert, J. A.; Tong, Y.; Mutz, N.; Vollmer, M.; Fischer, S.; Milowska, K. Z.; García Cortadella, R.; Nickel, B.; Cardenas-Daw, C.; Stolarczyk, J. K.; Urban, A. S.; Feldmann, J. *Nano Lett.* **2015**, *15*, 6521-6527.
25. Hintermayr, V. A.; Richter, A. F.; Ehrat, F.; Döblinger, M.; Vanderlinden, W.; Sichert, J. A.; Tong, Y.; Polavarapu, L.; Feldmann, J.; Urban, A. S. *Adv. Mater.* **2016**, *28*, 9478-9485.
26. Weidman, M. C.; Seitz, M.; Stranks, S. D.; Tisdale, W. A. *ACS Nano* **2016**, *10*, 7830-7839.
27. Shamsi, J.; Dang, Z.; Bianchini, P.; Canale, C.; Stasio, F. D.; Brescia, R.; Prato, M.; Manna, L. *J. Am. Chem. Soc.* **2016**, *138*, 7240-7243.
28. Weidman, M. C.; Goodman, A. J.; Tisdale, W. A. *Chem. Mater.* **2017**, *29*, 5019-5030.
29. Liu, J.; Xue, Y.; Wang, Z.; Xu, Z.-Q.; Zheng, C.; Weber, B.; Song, J.; Wang, Y.; Lu, Y.; Zhang, Y.; Bao, Q. *ACS Nano* **2016**, *10*, 3536-3542.
30. Dou, L.; Wong, A. B.; Yu, Y.; Lai, M.; Kornienko, N.; Eaton, S. W.; Fu, A.; Bischak, C. G.; Ma, J.; Ding, T.; Ginsberg, N. S.; Wang, L.-W.; Alivisatos, A. P.; Yang, P. *Science* **2015**, *349*, 1518-1521.
31. Tyagi, P.; Arveson, S. M.; Tisdale, W. A. *J. Phys. Chem. Lett.* **2015**, *6*, 1911-1916.
32. Pan, A.; He, B.; Fan, X.; Liu, Z.; Urban, J. J.; Alivisatos, A. P.; He, L.; Liu, Y. *ACS Nano* **2016**, *10*, 7943-7954.
33. Tong, Y.; Ehrat, F.; Vanderlinden, W.; Cardenas-Daw, C.; Stolarczyk, J. K.; Polavarapu, L.; Urban, A. S. *ACS Nano* **2016**, *10*, 10936-10944.
34. Levchuk, I.; Herre, P.; Brandl, M.; Osvet, A.; Hock, R.; Peukert, W.; Schweizer, P.; Spiecker, E.; Batentschuk, M.; Brabec, C. J. *Chem. Commun.* **2017**, *53*, 244-247.
35. Wang, Y.; Li, X.; Sreejith, S.; Cao, F.; Wang, Z.; Stuparu, M. C.; Zeng, H.; Sun, H. *Adv. Mater.* **2016**, *28*, 10637-10643.
36. Jagielski, J.; Kumar, S.; Wang, M.; Scullion, D.; Lawrence, R.; Li, Y.-T.; Yakunin, S.; Tian, T.; Kovalenko, M. V.; Chiu, Y.-C.; Santos, E. J. G.; Lin, S.; Shih, C.-J. *Sci. Adv.* **2017**, *3*.
37. Zhang, F.; Zhong, H.; Chen, C.; Wu, X.-g.; Hu, X.; Huang, H.; Han, J.; Zou, B.; Dong, Y. *ACS Nano* **2015**, *9*, 4533-4542.
38. Tessier, M. D.; Biadala, L.; Bouet, C.; Ithurria, S.; Abecassis, B.; Dubertret, B. *ACS Nano* **2013**, *7*, 3332-3340.

39. Tong, Y.; Bohn, B. J.; Bladt, E.; Wang, K.; Müller-Buschbaum, P.; Bals, S.; Urban, A. S.; Polavarapu, L.; Feldmann, J. *Angew. Chem. Int. Ed.* **2017**, *56*, 13887-13892.
40. Herz, L. M. *Annu. Rev. Phys. Chem.* **2016**, *67*, 65-89.
41. Naeem, A.; Masia, F.; Christodoulou, S.; Moreels, I.; Borri, P.; Langbein, W. *Phys. Rev. B* **2015**, *91*.
42. Bohn, B. J.; Simon, T.; Gramlich, M.; Richter, A. F.; Polavarapu, L.; Urban, A. S.; Feldmann, J. *ACS Photonics* **2017**, *5*, 648-654.
43. Tanaka, K.; Kondo, T. *Sci. Technol. Adv. Mater.* **2003**, *4*, 599-604.
44. Li, J.; Luo, L.; Huang, H.; Ma, C.; Ye, Z.; Zeng, J.; He, H. *J. Phys. Chem. Lett.* **2017**, *8*, 1161-1168.
45. Huang, H.; Polavarapu, L.; Sichert, J. A.; Susha, A. S.; Urban, A. S.; Rogach, A. L. *NPG Asia Mater.* **2016**, *8*, e328.
46. Herz, L. M. *Annu. Rev. Phys. Chem.* **2016**, *67*, 65-89.
47. Miyata, A.; Mitioglu, A.; Plochocka, P.; Portugall, O.; Wang, J. T.-W.; Stranks, S. D.; Snaith, H. J.; Nicholas, R. J. *Nat. Phys.* **2015**, *11*, 582-587.
48. Yao, E.-P.; Yang, Z.; Meng, L.; Sun, P.; Dong, S.; Yang, Y.; Yang, Y. *Adv. Mater.* **2017**, *29*.
49. Yang, D.; Zou, Y.; Li, P.; Liu, Q.; Wu, L.; Hu, H.; Xu, Y.; Sun, B.; Zhang, Q.; Lee, S.-T. *Nano Energy* **2018**, *47*, 235-242.
50. Giansante, C.; Infante, I. *J. Phys. Chem. Lett.* **2017**, *8*, 5209-5215.
51. Eperon, G. E.; Jedlicka, E.; Ginger, D. S. *J. Phys. Chem. Lett.* **2018**, *9*, 104-109.
52. Aneesh, J.; Swarnkar, A.; Kumar Ravi, V.; Sharma, R.; Nag, A.; Adarsh, K. V. *J. Phys. Chem. C* **2017**, *121*, 4734-4739.

TOC Graphic:

